Tuning the Quantum-Well Structure of Single-Crystal Layered Perovskite Heterostructures

Arundhati P. Deshmukh,[†,|] Yinan Chen,[§,|] Jamie L. Cleron,[†] Monique Tie,[‡] Jiajia Wen,[‖] Tony F. Heinz,[#,‡] Marina R. Filip,[§,*] Hemamala I. Karunadasa[†,‖,*]

[†]Department of Chemistry, Stanford University, Stanford, CA – 94305, USA. [§]Department of Physics, University of Oxford, Oxford OXI 3PU, UK. [‡]Stanford PULSE Institute, SLAC National Accelerator Laboratory, Menlo Park, CA – 94025, USA. [‖]Stanford Institute for Materials and Energy Sciences, SLAC National Accelerator Laboratory, Menlo Park, CA – 94025, USA. [#]Department of Applied Physics, Stanford University, Stanford, CA – 94305, USA.

[|]Equal contribution

KEYWORDS: Halide perovskites, chiral perovskites, interlayer excitons, Type-I and Type-II quantum-well heterostructure, second harmonic generation

ABSTRACT: Single-crystal layered perovskite heterostructures provide a scalable platform for potentially realizing emergent properties recently seen in mechanically stacked monolayers. We report two new layered perovskite heterostructures $M_2(PbCl_2)(AMCHC)_2(PbCl_4)\cdot 2H_2O$ (**1_M** where M = Na^+, Li^+; AMCHC = $^+NH_3CH_2C_6H_{10}COO^-$) crystallizing in the chiral, polar space group *C*2. The heterostructures exhibit alternating layers of a lead-chloride perovskite and an intergrowth comprising corner-sharing $PbCl_4(\eta^2\text{-}COO)_2$ polyhedra with bridging equatorial chlorides and terminal axial oxygen ligands. Small alkali metal cations and water molecules occupy the cavities between the polyhedra in the intergrowth layer. The heterostructures display wide bandgaps and two closely spaced excitonic features in their optical spectra and strong second harmonic generation. The calculated band structure of **1_Na** features a Type-I quantum-well structure, where the electron-hole correlation function corresponding to the lowest excited state points to electron-hole pairs localized within a single inorganic layer (intralayer excitons), as seen in typical layered halide perovskites. In contrast, calculations show that **1_Li** adopts a Type II quantum-well structure, with electrons and holes in the lowest-excited state residing in different inorganic layers (interlayer excitons). Calculations on model complexes suggest that these changes in band alignment, between Type-I and Type-II quantum-well structures, are driven by the placement of the alkali metal and the orientation of the water molecules changing the electrostatic potential-energy profiles of the heterostructures. Thus, this study sets the stage for accessing different alignments of the perovskite and intergrowth bands in bulk perovskite heterostructures that self-assemble in solution.

INTRODUCTION

Heterostructures comprising peeled and restacked monolayers of 2D van der Waals solids have been shown to host emergent properties such as correlated excitonic states, moiré superlattice effects, and exciton condensates.[1–4] Type-I and Type-II quantum-well heterostructures are characterized by the relative positioning of the band extrema of the neighboring heterolayers. In Type-I quantum wells, the lowest-energy excitons, created by excitations across the bandgaps of the individual layers, typically relax to the smaller-gap layer (Figure 1A). In contrast, when Type-II heterostructures are excited across the bandgaps of each layer, the electrons and holes undergo ultrafast charge transfer across the adjacent layers, forming spatially separated excitons across the neighboring layers (Figure 1B).[5] Such interlayer excitons were initially seen in hetero-bilayer flakes of transition metal dichalcogenides such as $MoSe_2/WSe_2$ and $MoS_2/MoSe_2$.[5,6] Interlayer excitons feature long lifetimes, low binding energies, and the ability to form high-density exciton condensates, opening intriguing potential applications in catalysis, optoelectronics, and quantum information science.[4,7]

The ability to tune the electronic structure from Type-I to Type-II through the application of an electric field or strain, pro-

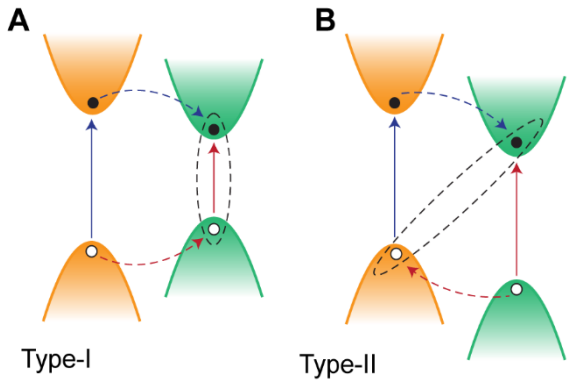

Figure 1. Schematic examples of a A) Type-I and B) Type-II quantum-well electronic structure in a bulk perovskite heterostructure. Solid red and blue arrows denote the intralayer optical excitations within the perovskite (green) and intergrowth (yellow) layers, respectively. In (A), the lowest-energy exciton (dashed oval) occurs within the perovskite layers. In (B), the lowest-energy exciton forms across perovskite and intergrowth layers via charge transfer of the photoexcited electrons and/or holes as denoted by dashed blue and red arrows, respectively.

vides still greater control over the exciton.[8–10] Typical fabrication methods for such hetero-layers involve layer-by-layer exfoliation and mechanical deposition, multistep chemical vapor deposition of one layer at a time, or molecular-beam epitaxy using specialized instrumentation.[3,11] Although impressive advances have been made in controlling these architectures, these approaches do not readily lead to inexpensive, scalable, and reproducible syntheses of well-defined interfaces.[3,11,12] This motivates the development of syntheses for multi-layered quantum-well heterostructures through one-pot, assembly reactions. Furthermore, the reversible reactions that occur in ionic solids in solution are conducive for forming single crystals, where the precise 3D atomic coordinates of the interfaces can be resolved through single-crystal X-ray diffraction.

Halide perovskites are well-known for their relatively low-temperature and scalable solution-state syntheses.[13] The dimensionally reduced 2D halide perovskites, have been studied for their quantum-well electronic structures since the 1980s,[14] yielding both free excitonic[15] and self-trapped excitonic[16] luminescence from the inorganic layers.[17] Most of the organoammonium molecules used in 2D perovskites lead to a Type-I quantum-well structure,[14,15,18,19] where the inorganic layers have smaller bandgaps than the HOMO-LUMO gap of the organic molecules. However, there are a few examples of highly conjugated dye molecules in the organic layers affording a Type-II bulk quantum-well structure, with excitation transfer from the inorganic layers to the discrete molecules in the organic layers.[20–23]

Our group recently devised a synthetic method for the self-assembly of heterostructures comprising halide perovskite layers interleaved with layers of a different inorganic solid (an intergrowth).[24] Replacing the organoammonium of typical 2D halide perovskites with a hetero-bifunctional organoammonium led to the self-assembly of layered heterostructure crystals where the ammonium group templates the perovskite layer and the second functional group dictates the connectivity of the intergrowth layer.[24,25] The soft perovskite framework can withstand significant structural distortions,[26] enabling a variety of non-perovskite structures, which may not exist otherwise, to be stabilized as intergrowths within the heterostructures. This approach led to the realization of heterostructures that mostly retained the quantum confinement properties of the parent 2D perovskites. Interestingly, electronic structure calculations of the heterostructure $(Pb_2Cl_2)(CYS)_2PbCl_4$ (CYS = $^+NH_3(CH_2)_2S^-$) showed a valence band maximum comprising states from the perovskite and intergrowth layers and a conduction band minimum formed with mostly perovskite states, suggesting the possibility of accessing interlayer excitons.[24] However, the calculated lowest-energy exciton wavefunction showed predominant intra-layer character with only slight delocalization between perovskite and intergrowth layers.

Motivated by this electronic structure, we sought a clearer spatial separation of the electron and hole between different layers and the realization of a true Type-II quantum-well electronic structure in a halide perovskite heterostructure. Such a perovskite would open new avenues for realizing the emergent properties arising from Type-II quantum wells in a highly tunable bulk material. The choice of the carboxylate group as the second functional group was informed by previous work where the carboxylate group templated molecular clusters within a layered perovskite[27] as well as non-perovskite lead-halide layered structures with similar excitonic properties as those seen in 2D lead-halide perovskites.[28,29] Herein, we present two new Pb-based heterostructures with a Pb-Cl perovskite layer and a Pb-Cl-carboxylate intergrowth, where both the zwitterionic organoammonium and a small H_2O-bound alkali metal cation (Na^+, Li^+) template the polar, chiral heterostructures. We see strong second harmonic generation from these heterostructures and describe how the choice of alkali metal cation changes the

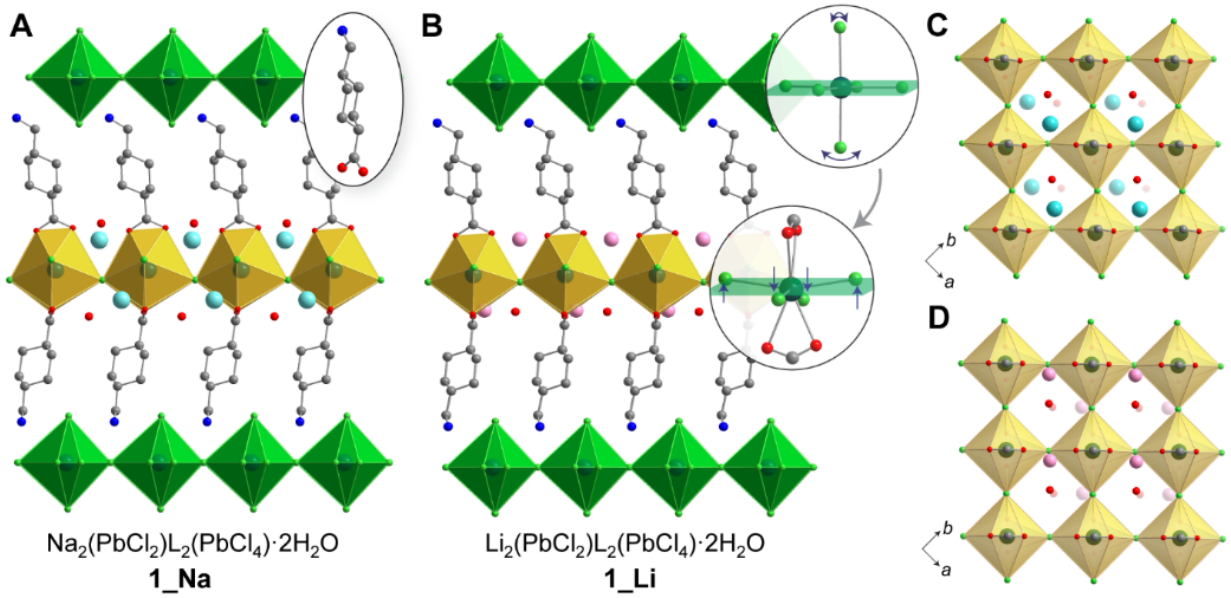

Figure 2. Single-crystal X-ray diffraction (SC-XRD) structures of A) $Na_2(PbCl_2)(AMCHC)_2(PbCl_4)\cdot 2H_2O$ (**1_Na**), and B) $Li_2(PbCl_2)(AMCHC)_2(PbCl_4)\cdot 2H_2O$ (**1_Li**). The perovskite and intergrowth layer Pb-centered polyhedra are shaded green and yellow, respectively. In (B), the H_2O molecule above the intergrowth layer is eclipsed by the Li cation. The inset in (A) shows the AMCHC ligand and the inset in (B) shows the conceptual derivation of the intergrowth layer binding motif $PbCl_4(\eta^2\text{-}COO)_2$ from a $PbCl_6$ octahedron. Curved arrows represent the bifurcation of the apical Pb–Cl bonds and straight arrows represent out-of-plane distortions of the bridging Pb–Cl bonds. Face-on views of the intergrowth layer in C) **1_Na** and D) **1_Li** with the atoms below the layer denoted by greater transparency. Atom colors: Pb: teal; Cl: green; Na: cyan, O: red; N: blue; C: grey; Li: pink. Hydrogen and disordered atoms are omitted for clarity.

calculated electronic structure of the material from a Type-I (Na^+) to a Type-II (Li^+) bulk quantum-well structure.

RESULTS AND DISCUSSION

1. Synthesis and structure. Mild heating of $PbCl_2$ and *trans*-(4-aminomethyl)cyclohexanecarboxylic acid (AMCHC) in concentrated, aqueous NaCl or LiCl yields a colorless solution. Slow evaporation of the solvent affords transparent plate-like crystals of $M_2(PbCl_2)(AMCHC)_2(PbCl_4)\cdot 2H_2O$ denoted as **1_Na** (M = Na^+) and **1_Li** (M = Li^+) (see the Supporting Information). Single-crystal X-ray diffraction (SC-XRD) shows a layered heterostructure with alternating perovskite $[PbX_4]^{2-}$ and non-perovskite $[PbX_2(\eta^2\text{-}COO)_2]^{2-}$ layers (Figure 2A-B; crystallographic data are in Table S3). We refer to these alternating layers as the perovskite layer (shaded green) and the intergrowth layer (shaded yellow). Both the heterostructures crystallize in a low-symmetry monoclinic *C*2 space group belonging to the polar point group C_2. Such space groups are known to show interesting band structures with Rashba-Dresselhaus splitting, second harmonic generation, and chiro-optical properties due to the absence of bulk inversion symmetry (further discussed later).[30,31]

Elemental analysis (Tables S4-S5) supports the formula obtained from SC-XRD. In analogy to an ammonium group occupying the cavity between the metal-halide octahedra on each side of the perovskite layer, an H_2O-bound Na^+ or Li^+ cation occupies the cavity between the corner-sharing polyhedra on each side of the intergrowth layers (Figure 2C). Powder X-ray diffraction (PXRD) confirms the phase purity of both heterostructures (Figure S2). Infrared spectroscopy (Figure S3) shows reduced spacing between the peaks corresponding to the symmetric and asymmetric carboxylate stretching modes in the heterostructure compared to those of the free zwitterionic ligand, a signature of bidentate binding of the carboxylate group to the metal ion.[32] In addition, we observe peaks corresponding to the O–H stretch and H–O–H bend of H_2O in both the heterostructures (absent in the spectrum of the ligand), assigned to the crystallographic water molecules (Figure S3). Thermogravimetric analysis (Figure S4) shows a mass loss step of 36.8 g/mol (3.6%) and 35.6 g/mol (3.5%) at ca. 100 °C for **1_Na** and **1_Li**, respectively, reflecting the loss of two water molecules per formula unit (calculated: 3.5% and 3.6% based on formula weights of 1023.55 and 991.46 g/mol for **1_Na** and **1_Li**, respectively). Pulverizing crystals of **1_Li** in ambient air led to a large broad peak in the O–H stretching region of the IR spectrum due to surface adsorbed water, although PXRD data showed no structural changes or loss of crystallinity even after a day of air exposure (Figure S6). Specific heat capacity data (Figure S5) do not show any sharp peaks from 4 - 250 K, indicating the absence of phase transitions in this temperature range.

The intergrowth layer can be described as corner-sharing 8-coordinate $PbCl_4(\eta^2\text{-}COO)_2$ polyhedra, which can be derived from a regular $PbCl_6$ octahedron by bifurcating the apical Pb–Cl bonds into two bonds with the bidentate carboxylate group as schematically depicted in the inset of Figure 2B. The O–C–O plane of the carboxylate groups at the top and bottom of each layer are mutually orthogonal. The local coordination environment of Li^+ and Na^+ can be described as a distorted trigonal pyramid with three O atoms in the basal plane and one Cl at the apex (Figure S7). Notably, the Pb–Cl connectivity within the layers of the intergrowth is like that of a perovskite.

As shown in the inset of Figure 2B, the Pb–Cl bonds parallel to the O–C–O plane are pushed out of the Pb plane, leading to

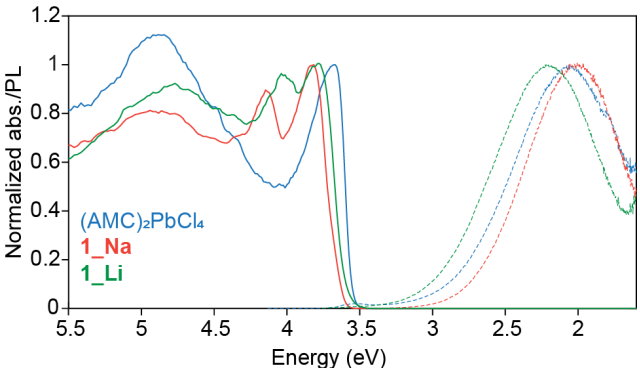

Figure 3. Normalized absorption (abs.) spectra (solid lines) converted from diffuse reflectance using the Kubelka-Munk transformation and photoluminescence (PL) spectra (dashed lines) of powders of the 2D perovskite $(AMC)_2PbCl_4$ (blue), **1_Na** (red), and **1_Li** (green) at room temperature.

significant out-of-plane distortions in the intergrowth layer. We calculated the octahedral distortion parameters (D_{in}, D_{out}) to quantitatively compare the distortions in both the structures using a previously reported procedure.[33] Briefly, D_{in} and D_{out} refer to the deviation of the Pb–(μ-Cl)–Pb bond angle from linearity, $D_{in} = 180° - \theta_{in}$ and $D_{out} = 180° - \theta_{out}$ where θ_{in}, θ_{out} are the in- and out-of-plane projections of the bond angle. The plane is defined by three non-colinear Pb atoms within the inorganic layers. To check whether the distortions in the perovskite layers are inherent to the parent 2D perovskite or appear only in the heterostructure, we synthesized the 2D perovskite $(AMC)_2PbCl_4$ (AMC = $^+NH_3CH_2C_6H_{11}$) whose bromide analog was previously reported.[34] The ligand AMC is structurally similar to AMCHC except for the replacement of the COO^- group with a hydrogen (SC-XRD structure and PXRD data are shown in Figure S8). The perovskite layers in both the heterostructures show similar octahedral distortions as those in the 2D perovskite $(AMC)_2PbCl_4$ (Table S6), indicating that the heterostructure did not induce significant distortions in the perovskite layers. On the other hand, the intergrowth layer in **1_Na** has significantly higher in-plane as well as out-of-plane distortions as compared to the intergrowth of **1_Li**. These distortion parameters suggest that any changes in band dispersion between the heterostructures should arise from the intergrowth layers.

2. Optical properties. Diffuse reflectance spectra of powders of **1_Li**, **1_Na**, and $(AMC)_2PbCl_4$ show a high-energy absorption onset, just above 3.5 eV, consistent with the excitonic absorption onset of reported 2D Pb–Cl perovskites (Figure 3).[35] However, in contrast to the 2D perovskites, an additional excitonic peak is apparent in the spectra of **1_Li** and **1_Na**. Notably, even our previously reported Pb-based heterostructures, $(PbBr_2)_2(AMTP)_2PbBr_4$ (AMTP = 4-ammoniomethyl-tetrahydropyran) and $(Pb_2Cl_2)(CYS)_2PbCl_4$), displayed only one excitonic peak below the bandgap onset.[24] In the case of $(PbBr_2)_2(AMTP)_2PbBr_4$, which most resembles the structure of **1_Na** and **1_Li** with Pb-Br perovskite and Pb-Br intergrowth layers well-separated by an organic layer, a second excitonic peak was evident in both experimental and calculated spectra, but at energies higher than the heterostructure bandgap.

Based on the calculated band structures of **1_Na** and **1_Li** (section 3), we attribute the two closely spaced excitonic peaks to intralayer optical transitions within the perovskite and intergrowth layers. Unlike in our other reported heterostructures, the

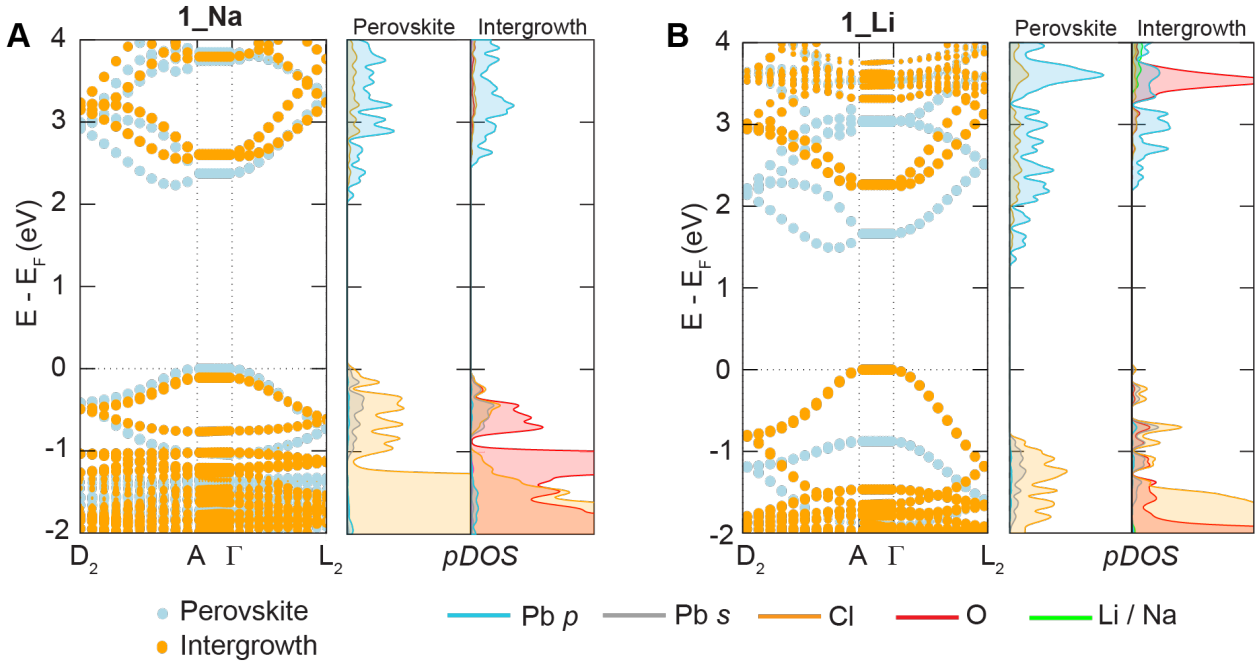

Figure 4. A) DFT-PBE band structure (left) and projected density of states (pDOS; right) for **1_Na**. B) DFT-PBE band structure (left) and pDOS (right) for **1_Li**. Blue and orange bands correspond to the electronic states from the perovskite and intergrowth layers, respectively. Color scheme for the pDOS: Pb p: blue; Pb s: gray; Cl: orange; O: red; Li/Na: green.

two excitonic peaks have relatively close energies, thereby giving rise to the double-peak feature in the optical absorption spectra. This band structure likely arises from both the perovskite and intergrowth layers having "perovskite-like" intralayer connectivity (i.e., a corner-sharing Pb-Cl square-net as shown in Figure 2C-D).

Powders of **1_Li**, **1_Na**, and $(AMC)_2PbCl_4$ all show broadband yellow-orange emission, as seen in other 2D Pb–Cl perovskites[35] and layered Pb–Cl hybrids.[28,29] The photoluminescence (PL) spectra are highly Stokes shifted (~ 1.6 – 1.8 eV) and broad with **1_Na** showing the highest Stokes shift of the three. Similar broad, Stokes shifted emission in 2D Pb–Cl and Pb–Br perovskites is attributed to exciton self-trapping.[36,37] We do not observe any PL intensity from sub-gap excitation for both **1_Na** and **1_Li** (Figure S9). Photoluminescence excitation (PLE) spectra qualitatively match the absorption spectra of the heterostructures and show no sub-gap features when probed at different regions of the broad emission (Figure S10). Cryogenic PL spectra for **1_Na** and **1_Li**, down to 78 K (Figure S11) show an increase in PL intensity and a narrowing peak width upon lowering the temperature (Figures S12-S13). PL decay curves at 77 K (Figure S14B and Table S9) show similar µs lifetimes for both **1_Na** and **1_Li** at a 560 nm emission wavelength. These combined data are consistent with exciton self-trapping.[36,37] Similar to other Pb–Cl 2D perovskites, we do not see PL from free excitons down to 78 K, suggesting a low-energy barrier for self-trapping.[33] We have previously shown the low barrier to self-trapping to be a common feature among all layered Pb-Cl 2D perovskites[35] and the Pb–Cl heterostructures appear to follow this trend. The CIE coordinates at 78 K (Figure S14A) depict a yellow-orange color of the broadband emission with **1_Na** being slightly redder than the emission in **1_Li**.

3. Band structure calculations. We calculated the band structures of **1_Na** and **1_Li** using density functional theory in the Perdew, Burke, Erznhof parametrization (DFT-PBE),[38,39] including spin-orbit coupling along the path D_2 (0.5, 0.5, 0.5)– A (0, 0, 0.5) – Γ(0, 0, 0) – L_2 (0, 0.5, 0.5) in reciprocal lattice units,[40] using atomic coordinates from the SC-XRD structures without relaxation (see the Supporting Information). Both heterostructures show a slightly indirect bandgap as shown in Figure 4, a consequence of the Rashba-Dresselhaus splitting.[30] This effect is expected given the absence of bulk inversion symmetry and is common among polar space groups such as *C*2.[30]

The electronic structures of **1_Na** and **1_Li** show separate manifolds of bands, derived from the perovskite and intergrowth layers, with roughly similar dispersion patterns as expected from their similar intra-layer Pb-Cl connectivity (Figure 4). In stark contrast with expectations from experimental optical absorption spectra, the electronic bandgaps calculated within DFT/PBE and the *GW* approximation[41,42] (see Supporting Information) for these two heterostructures differ by ca. 700-800 meV (the experimental absorption onset difference is ca. 50 meV; Table S10). Furthermore, **1_Na** shows a Type-I quantum-well band alignment, with the conduction band minimum (CBM) and valence band maximum (VBM) comprising electronic states from the perovskite layers. In contrast, **1_Li** shows a Type-II quantum-well band alignment with the VBM exclusively formed by electronic states from the intergrowth layer and states from the perovskite layer forming the CBM. The projected density of states (pDOS) for **1_Na** shows similar band-edge composition as for other layered lead-halide perovskites. In contrast, in **1_Li**, the VBM has contributions from O 2p, Pb 6s, and Cl 2p states from the intergrowth layer, whereas the CBM comprises mostly Pb 6p orbitals from the perovskite layer.

Since the Pb–Cl frameworks of **1_Na** and **1_Li** are relatively similar, and since the Li^+ and Na^+ cations do not contribute to electronic states at the band edges, this shift from a Type-I to

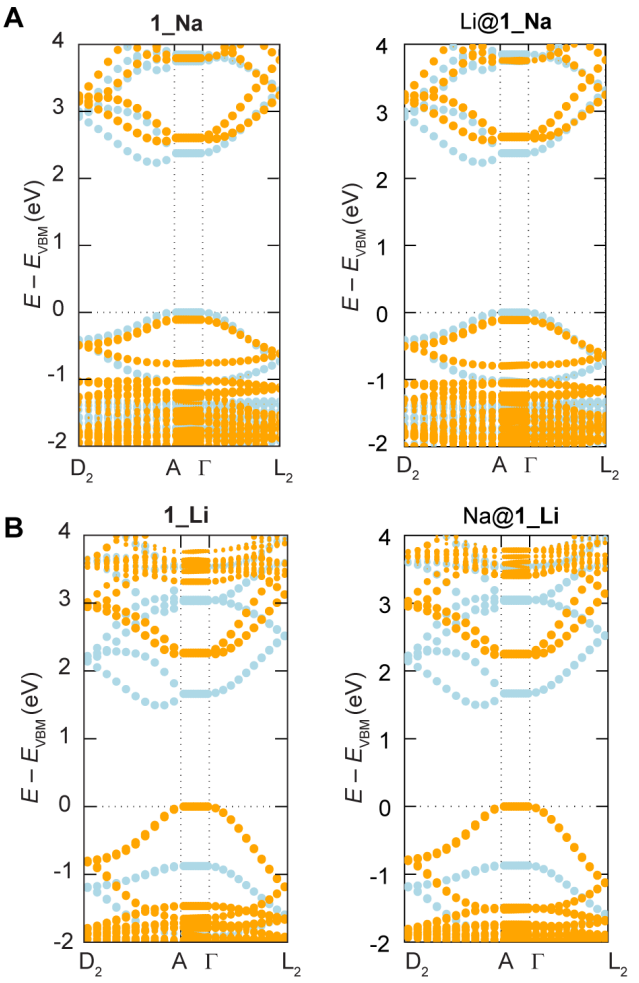

Figure 5. A) Band structures of **1_Na** (left) and of a model structure where the Na^+ is replaced with Li^+ (Li@**1_Na**; right). B) Band structures of **1_Li** (left) and of a model structure where the Li^+ replaced with Na^+ (Na@**1_Li**; right).

Type-II quantum-well band alignment is surprising. We investigated this shift by calculating the profile of the electrostatic potential, originating from the ions and electronic charge density, $V_{bare} + V_H$, respectively, along the layer stacking direction (see the Supporting Information). The potential-energy profiles of the perovskite layers are very similar, though those of the intergrowth layers show clear differences (Figure S15), suggesting that the band-alignment difference between **1_Na** and **1_Li** is driven by the intergrowth layers.

To investigate the origin of this effect, we calculated the band structures and potential-energy profiles of a series of model structures. We first replaced Na^+ with Li^+ in the structure of **1_Na** (Li@**1_Na**) and found that the band structure (Figure 5A) and potential-energy profile (Figure S16) do not significantly change. Likewise, replacing Li^+ with Na^+ in the structure of **1_Li** (Na@**1_Li**) does not significantly perturb the band structure (Figure 5B) or the potential-energy profile (Figure S15), indicating that the identity of the alkali metal alone does not change the band alignment.

The Na^+ and Li^+ cations occupy different positions relative to the intergrowth layer (Figure 2C-D). To test if the placement of the alkali cations in **1_Na** and **1_Li** affects band alignment, we then calculated the band structures of a series of model complexes where the Na^+, in the structure of **1_Na**, is gradually moved along a linear path to the approximate position occupied by Li^+, in the intergrowth of **1_Li** (a total displacement of 1.8 Å), while keeping the rest of the framework fixed to that **1_Na**. Indeed, as the Na^+ is displaced, we see the highest-filled and lowest-empty intergrowth-derived bands destabilize and the Type-I quantum-well structure of **1_Na** slowly convert to a Type-II quantum-well structure (Figure 6). The average potential-energy profile of the intergrowth layers of **1_Na** also gradually shifts as a function of Na^+ displacement (Figure S17a). Indeed, the calculated band offsets (energy differences between the valence-band maxima or conduction-band minima of the intergrowth-derived bands and perovskite-derived bands) for this series of structures show a nearly linear correlation with the volume-averaged potential energy of the intergrowth layer as a function of Na^+ displacement (Figure S17b). Since Na^+ sits deeper within the intergrowth layer as compared to Li^+, the electrostatic attraction between the positively charged alkali metal and negatively charged intergrowth layer may stabilize the intergrowth-derived bands in **1_Na** relative to those in **1_Li**. We thus propose that the position of the alkali metal cation relative to the intergrowth layer causes a large change in the electrostatic potential energy of the intergrowth layer, driving the change in the relative alignment of the intergrowth and perovskite bands, with the structural differences between the intergrowth frameworks (also likely templated by the alkali metals, Table S6) modulating band dispersion.

We then checked whether geometry optimization affected the computed band alignments of **1_Na** and **1_Li** (see Supporting Information for details). Performing unconstrained relaxation of the atomic positions and lattice parameters, including van der Waals interactions,[41] resulted in structures with unit-cell parameters similar to those from experiment (Table S11). Geometry optimization did not lead to large structural changes for **1_Na**, and the band alignment remained as Type I, with larger band offsets compared to those computed for the experimental structure (Figure S18). For **1_Li**, the Type-II band alignment is maintained upon structural relaxation, although the valence-band offset was reduced to 0.15 eV (compared to the 0.88 eV offset in the unrelaxed structure; Figure S18). This change could be traced to a reorientation of the H_2O molecules upon relaxation. In the SC-XRD structures of **1_Li** and **1_Na**, the H atoms in the H_2O molecules could not be located from the electron density difference maps and they were inserted in idealized positions and refined, resulting in H_2O molecules that appear to H-bond with the carboxylate oxygen atoms. Upon structural relaxation of **1_Li**, these H_2O molecules rotate to positions consistent with H-bonding with the chlorides of the intergrowth layer (Figure S20), with the angle between the plane of the H_2O molecule and the crystallographic (002) plane (which runs parallel to the inorganic layers) increasing from 10° to 47°. Note that if the structural relaxation was performed without including van der Waals interactions, the band alignment for **1_Li** changed to Type-I (with a small valence-band offset of 0.08 eV) whereas the alignment for **1_Na** remained Type-I (Figure S19). Given the sensitivity of the electronic structure to the orientation (dipole) of the H_2O molecules (Figure S21), we performed all subsequent calculations using the experimental crystal structures.

We computed the linear optical absorption spectra within the Bethe-Salpeter Equation framework, (see the Supporting Information).[42–45] The calculated absorption spectra for **1_Na** and **1_Li** (Figure 7 and Figure S22) offer an explanation for the discrepancy between calculated electronic bandgaps and measured

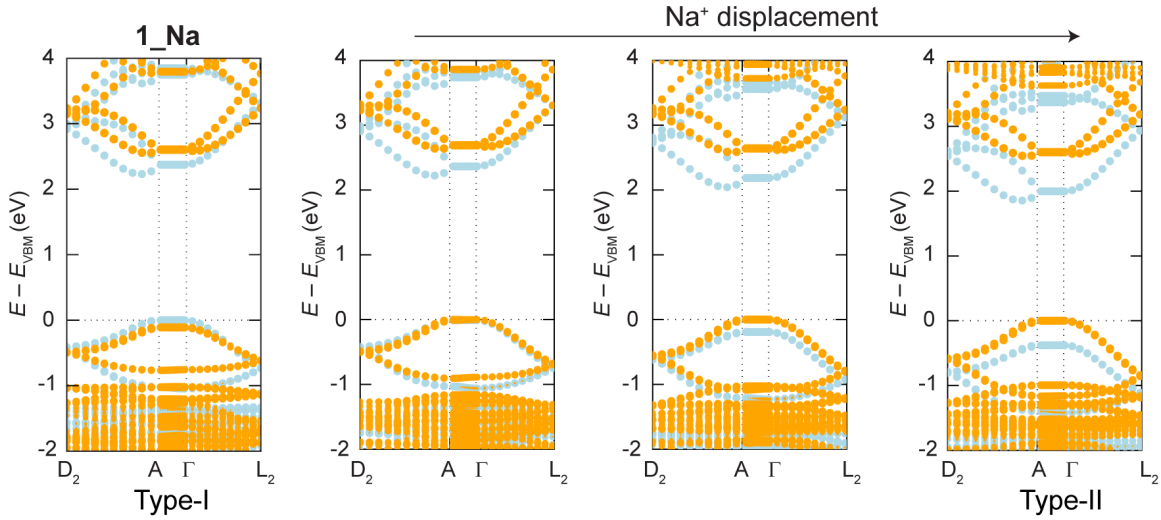

Figure 6. Band structures of **1_Na** (left) and of model structures where the Na^+ is gradually displaced towards the position occupied by Li^+ in the structure of **1_Li** showing the intergrowth-derived bands (orange) destabilize and the band structure shift from a Type-I to a Type-II quantum-well structure. The perovskite and intergrowth layer frameworks are kept fixed to those of **1_Na**.

optical absorption onsets. We find that both calculated spectra exhibit two bright excitonic peaks at the onset of optical absorption with similar energies (Figure S22). The calculated energies corresponding to these resonant peaks are underestimated with respect to experiment by approximately 0.7 eV (for both **1_Li** and **1_Na**). This is a result of a systematic underestimation of the quasiparticle bandgap, which has been observed more generally in G_0W_0 calculations with a DFT-PBE starting point for halide perovskites and other semiconductors and has been well-documented in recent literature.[46–49]

Despite these systematic errors, we observe good agreement between measured and calculated optical spectra for the two main peaks at the onset of absorption. First, the calculated optical absorption onsets of **1_Li** and **1_Na** have similar energies as seen from the unscaled spectra in Figure S22 (within 50 meV from each other, in good agreement with the 50 meV difference observed in the experiment, Table S10). Second, the separation between the two excitonic peaks in the experimental spectra is 250 meV and 320 meV for **1_Li** and **1_Na**, respectively, and that for the calculated spectra is 238 meV and 586 meV, respectively. One possible source for the slight discrepancy between these measured and calculated energy differences can be numerical convergence. As discussed in the Supporting Information, we estimate that the computational setup we have chosen achieves convergence of the excited-state energies within approximately 100 meV (Figure S1). Finally, in the case of **1_Li**, our calculations reveal several optical transitions with energies up to 0.5 eV below the main exciton peaks, and with low oscillator strengths (Figure S22). The presence of these dark excitons explains why the experimental optical absorption onsets, which only reflect the bright excitons, are similar for **1_Li** and **1_Na** despite the much larger difference between their calculated electronic bandgaps (Figure 4A-B).

4. Calculations of interlayer and intralayer excitons. In analogy to van der Waals stacks in 2D materials, we hypothesize that the Type-II quantum-well band structure in **1_Li** can facilitate the formation of low-energy interlayer excitons; this hypothesis is consistent with the prediction of several dark excited states with energies below the optical absorption onset of **1_Li**. To probe this, we calculated the electron-hole correlation function (ECF) using the approach introduced by Sharifzadeh et al.,[50] and previously applied to layered perovskites by Chen and Filip.[51] The ECF corresponds to the probability that the electron and hole are separated by a relative position vector **r**. Figure 8A depicts the normalized planar-averaged 1D ECF (integrated along the two in-plane directions) showing the projected electron-hole distance perpendicular to the layers for the lowest-energy excited states of **1_Na** (bright state) and **1_Li** (dark state), along with the lowest-energy bright state of **1_Li**; the detailed calculation is in the Supporting Information. Figure 8A shows that the highest-probability electron-hole distance perpendicular to the inorganic sheets in **1_Li** is similar to the separation between the perovskite and intergrowth layers. This indicates that the lowest-energy excited state in **1_Li** is an interlayer exciton. The average electron-hole distance along the direction perpendicular to the inorganic sheets $\langle r_{eh} \rangle_\perp = 14.9$ Å for **1_Li**, slightly larger than the separation between the perovskite and intergrowth layers (11.8 Å). On the other hand, $\langle r_{eh} \rangle_\perp = 3.2$ Å for the lowest-energy excited state of **1_Na**, which is similar to the thickness of the perovskite layer (~5.6 Å), indicating an intralayer exciton. Figure 8B-C illustrates the delocalization of a

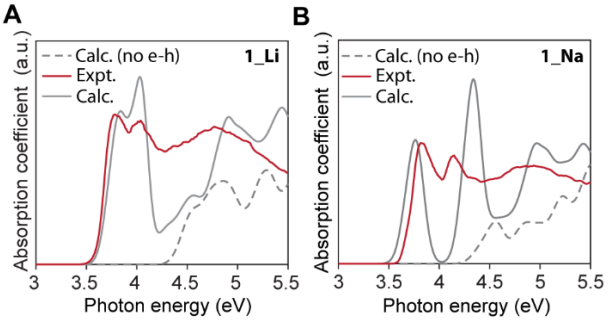

Figure 7. Calculated absorption spectra with (solid grey) and without (dashed grey) electron-hole interactions overlayed with the experimental diffuse reflectance spectra (red) for A) **1_Li** and B) **1_Na**. Both the calculated spectra were arbitrarily scaled along the *y*-axis and blue-shifted by 0.7 eV to overlay with the experimental spectra.

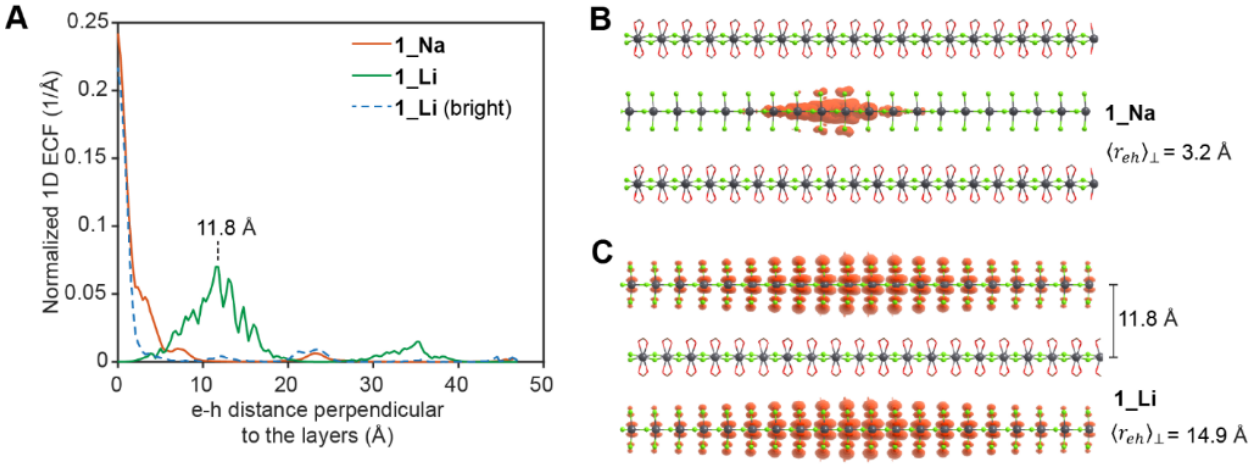

Figure 8. A) Normalized planar-averaged 1D electron-hole correlation function (ECF) as a function of the electron-hole distance in the direction perpendicular to the layers for the lowest-energy excited state of **1_Na** (red) and **1_Li** (green), along with the lowest-energy bright state of **1_Li** (dashed blue). Isosurfaces representing the spatial distribution of the photoexcited electron in the lowest-energy excited state in B) **1_Na** showing an intralayer exciton (hole fixed at center of the perovskite layer), and C) **1_Li** showing an interlayer exciton (hole fixed at the center of the intergrowth layer). The weighted average electron-hole separation perpendicular to the layers, $\langle r_{eh} \rangle_{\perp}$ (shown at the right) is significantly higher for **1_Li** compared to that of **1_Na**, and larger than the distance between the perovskite and intergrowth layers. Pb and Cl atoms are represented by gray and green spheres, respectively. The carboxylate group is denoted by red sticks; the rest of the ligands, water molecules, and alkali metal cations are omitted for clarity.

photoexcited electron corresponding to these lowest-energy exciton states in **1_Na** and **1_Li**, when the associated hole is localized to a specific position in the perovskite or intergrowth layer, respectively, (the extended isosurface for **1_Li** is shown in Figure S23 a). Out-of-plane exciton delocalization was also recently predicted in 2D Pb–I perovskites with Type-I quantum-well electronic structures, with interlayer spacing of ~10.5 Å.[51] Although, in that case, the highest-probability exciton still remained within the same layer, with a decaying probability across layers. The notable difference with **1_Li** is that the correlated electron-hole pair, corresponding to the lowest-energy excited state, is delocalized completely across neighboring layers (electrons in the perovskite layer and holes in the intergrowth), fully consistent with a Type-II quantum-well structure.

The lowest-energy exciton in **1_Na**, lying 0.932 eV below the quasiparticle bandgap, is intralayer, and optically bright (Figure S22). In contrast, the lowest-energy exciton in **1_Li**, which lies 0.380 eV below the quasiparticle bandgap, is interlayer, with an oscillator strength at least three orders of magnitude lower than those of the other states visible in the optical spectrum. The lowest-energy bright excited state in **1_Li** (corresponding to the first resonant peak of the optical absorption spectrum) is an intralayer exciton with the electron-hole pair localized within a single layer (Figure 8A, dashed blue line) with $\langle r_{eh} \rangle_{\perp} = 3.0$ Å (the isosurface is shown in Figure S23 b). This bright state in **1_Li** lies 0.355 eV higher in energy than the lowest-energy dark exciton as shown in Figure S22 (0.025 eV below the quasiparticle bandgap). Interlayer excitons typically have very low oscillator strengths due to reduced wavefunction overlap between the electron and hole, and are usually probed using ultrafast transient absorption or PL under external stimuli.[5] However, in this case, fast self-trapping appears to dominate the excited-state dynamics, making it difficult to optically probe the presumably slower formation of the predicted interlayer excitons in **1_Li**. Fluctuations of the dipole moment of the water molecule at room temperature may also change the band offsets from those calculated at 0 K. Future investigations using ultrafast pump-probe experiments could shed more light on the unusual excited-state of **1_Li**.

5. Non-linear optics (NLO). The wide bandgap and chiral polar space group of **1_Li** and **1_Na** motivated us to test the heterostructures for second harmonic generation (SHG).[52] SHG experiments were performed on single crystals using ultrafast pulses at 1030 nm, whose second harmonic (515 nm) is well below the absorption onsets for both the heterostructures (~350 nm). We recorded the intensity of the reflected second-harmonic radiation polarized parallel to the pump polarization as a function of the pump polarization. The power dependence of the maximum SHG signal for both the heterostructures is shown in Figure 9 along with comparison against crystalline quartz as a reference.[53,54] We obtain quadratic power dependence for both the heterostructures and the quartz reference, consistent with a second-order optical process (a detailed list of fit parameters is shown in Table S13). In addition, both **1_Na** and **1_Li** show orders of magnitude higher SHG intensities when compared to the response from quartz under the same excitation conditions (~10^3 times at 10 mW average power). The effective second-order susceptibility coefficient, d_{eff}, provides a quantitative comparison metric across samples. We evaluated d_{eff} for both the heterostructures using a relative method described previously.[55] Using the reported d_{eff} value for quartz,[56] we estimate the d_{eff} for **1_Na** to be 11.2 pm/V and the d_{eff} of **1_Li** to be 14.9 pm/V, which are ~37 and ~50 times that of quartz, respectively, at 10 mW average power. Although we do not take phase matching into account, these values represent lower-bound estimates based on the measured intensities (details are in the Supporting Information). The obtained d_{eff} lower bounds are significantly higher than d_{eff} values previously reported for lead-halide perovskites, e.g., (phenylmethylammonium)$_2$PbCl$_4$ (1.4 pm/V)[57] (cyclohexylammonium)$_2$PbBr$_4$ (1.2 pm/V),[58] and comparable to that of $AgGaS_2$ (reported 11-13 pm/V at similar fundamental frequency), a commercially used NLO material.[59] Thus, our initial investigations indicate the presence of strong SHG in both the chiral non-centrosymmetric heterostructures.

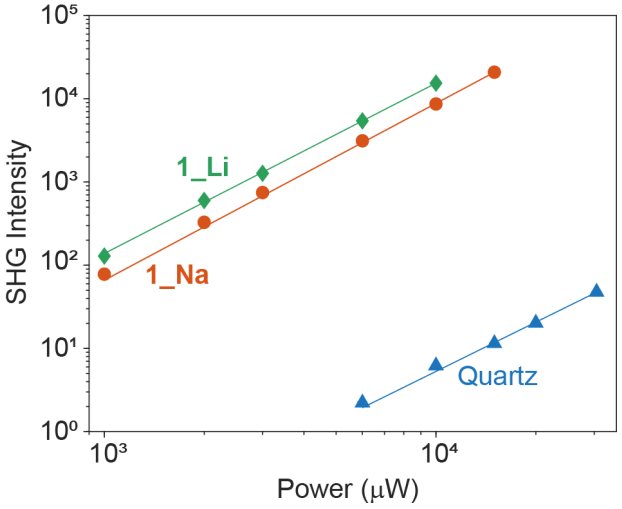

Figure 9. Second harmonic generation (SHG) as a function of incident power for **1_Li** (green diamonds) and **1_Na** (orange circles). SHG of crystalline quartz (blue triangles) under the same experimental conditions is shown for comparison. Solid lines are fits to $y = ax^b$, $\lambda_\omega = 1030$ nm. Fitting parameters are given in Table S13.

Notably, both **1_Na** and **1_Li** crystallize in a chiral space group without the presence of a chiral organic molecule or helical symmetry, which is rare among hybrid lead-halides[53,55,60–62] with the few exceptions containing large aromatic ligands[22,63,64] or halogen substituted ligands.[65,66] We attribute the chiral polar structure and the strong SHG arising from it to the low-symmetry structure of the intergrowth layer, which has so far only been isolated within the layered perovskite heterostructure.

We performed polarization dependent SHG for multiple spots across 3–4 different crystals, which showed a surprising spot-dependent response with either 2-, 4- or 6-lobe patterns (Figure S24). All the polarization patterns show 2-fold symmetry. We attribute this behavior to the presence of stacking faults or inherent polarization dependence within the crystals as seen from optical microscope images with a polarizer (Figure S25).[67] The polarization response could also be complicated by the presence of ferroelectricity due to the polar space group.[68] Nevertheless, the polarization dependence hints that SHG can be a powerful technique to map crystal domains or local strain within these heterostructures.[67]

CONCLUSIONS

We report two new layered perovskite heterostructures with bidentate carboxylate bound $PbCl_4(\eta^2\text{-}COO)_2$ polyhedra in the intergrowth layer. An H_2O-bound small alkali metal cation (Na^+, Li^+) occupies the cavity between the corner-sharing polyhedra in the intergrowth layers. The chiral, non-centrosymmetric, heterostructures exhibit strong SHG, where local domain mapping with microscopic SHG polarization can be explored in the future.

The calculated band structures of **1_Na** and **1_Li** feature manifolds of perovskite-based and intergrowth-based bands with similar dispersion patterns, likely due to the "perovskite-like" Pb–Cl connectivity within both layers. This unique band structure gives rise to two excitonic bands below the heterostructure bandgap, seen in both experimental and calculated spectra and attributed to intra-layer excitations.

Despite the similar band dispersion patterns in **1_Na** and **1_Li**, the alkali metal cation appears to have a drastic effect on the relative alignment between perovskite-derived and intergrowth-derived bands. The calculated band structure of **1_Li** shows a Type-II bulk quantum-well structure in contrast to the Type-I bulk quantum-well structure in **1_Na**. Calculations on a series of model complexes indicate that the position of the alkali metal, and not its identity, effects this transformation in band alignment by changing the electrostatic potential-energy profile of the intergrowth layers. We further find that the band alignment is highly sensitive to the dipole moment of the H_2O molecules, fully consistent with the electrostatic arguments above. Notably, the prediction that small alkali cations and polar molecules can modulate the relative alignment of the perovskite and intergrowth bands may offer a powerful new synthetic handle for tuning the quantum-well structure of these self-assembling heterostructures.

First-principles calculations of optical excitations for the experimental structure of **1_Li** predict that the lowest-energy exciton in the Type-II heterostructure corresponds to an electron-hole pair completely delocalized across neighboring inorganic layers (an interlayer exciton), unlike in previously reported 2D perovskites where the highest-probability electron-hole separation is intralayer.[24,51] In contrast to prior examples of Type-II bulk quantum-well structures in 2D halide perovskites with excitation transfer to conjugated organic molecules,[20,21] here the calculated electron and hole wavefunctions are delocalized between different inorganic layers with extended electronic bands. Further work is needed to fully understand the novel and complex excited-state energy landscape in **1_Li**, where like in layered Pb–Cl perovskites,[35] self-trapping appears to dominate the excited-state dynamics. However, our detailed study of how the placement of alkali cations and polar molecules can change the band alignment in **1_Li** and **1_Na** sets the foundation for accessing interlayer excitons and other emergent phenomena in self-assembled bulk materials, where chemical tunability and specificity can provide new ways to control the interlayer interactions.

ASSOCIATED CONTENT

Supporting Information

The Supporting Information is available free of charge at http://pubs.acs.org.

Experimental section, computational methods, powder X-ray diffraction, elemental analysis, thermogravimetric analysis, infrared spectroscopy, specific heat capacity, low temperature photoluminescence, CIE coordinates, supporting optical properties calculations, calculation of second order susceptibility coefficients, polarization dependent SHG.

Accession Codes

Crystallographic Information Files (CIFs) for the reported structures are deposited in the Cambridge Crystallographic Data Center (CCDC) with accession codes 2445552-2445554. These data can be obtained free of charge via www.ccdc.cam.ac.uk/data_request/cif, or by emailing data_request@ccdc.cam.ac.uk, or by contacting The Cambridge Crystallographic Data Centre, 12 Union Road, Cambridge CB2 1EZ, UK; fax: +44 1223 336033.

Data Availability

Raw data for the graphs reported in this paper are deposited in the Stanford Digital Repository (SDR) available free of charge.

AUTHOR INFORMATION

Corresponding Author

*Email: hemamala@stanford.edu; marina.filip@physics.ox.ac.uk

Notes

Authors declare no competing interest.

ACKNOWLEDGMENTS

This work was funded by the Brown Science Foundation and the National Science Foundation (DMR–2428278). APD acknowledges a TomKat Center Postdoctoral Fellowship in Sustainable Energy. MRF and YC acknowledge funding from the UK Engineering and Physical Sciences Research Council (EPSRC). YC and MRF acknowledge access to computational resources of the Oak Ridge Leadership Computing Facility, a U.S. Department of Energy (U.S. DOE) Office of Science User Facility supported under Contract DE-AC05-00OR22725 (accessed through the INCITE and SummitPlus programs). YC and MRF also acknowledge the EuroHPC Joint Undertaking for awarding access to the EuroHPC supercomputer LEONARDO Booster, hosted by CINECA (Italy) and the LEONARDO consortium through an EuroHPC Regular Access call. J.L.C. was supported by a Stanford Graduate Fellowship. Research by M. T. and T. F. H. was supported by the U.S. DOE under FWP #SCW0063 at SLAC as part of the AMOS program, Chemical Sciences, Geosciences, and Biosciences Division, Basic Energy Sciences. We thank Dr. Simon Teat, Advanced Light Source, LBNL for crystallography assistance, and Dr. Peter Djurovich University of Southern California, for time-resolved PL analysis. SC-XRD studies were performed either at the Advanced Light Source (Beamline 12.2.1) at the Lawrence Berkeley National Laboratory (LBNL) or at Stanford Nano Shared Facilities, supported by the NSF (award ECCS-1542152).

REFERENCES

(1) Wang, P.; Jia, C.; Huang, Y.; Duan, X. Review Van Der Waals Heterostructures by Design : From 1D and 2D to 3D. *Matter* **2021**, *4* (2), 552–581. https://doi.org/10.1016/j.matt.2020.12.015.

(2) Castellanos-Gomez, A.; Duan, X.; Fei, Z.; Gutierrez, H. R.; Huang, Y.; Huang, X.; Quereda, J.; Qian, Q.; Sutter, E.; Sutter, P. Van Der Waals Heterostructures. *Nat. Rev. Methods Primer* **2022**, *2* (1), 1–19. https://doi.org/10.1038/s43586-022-00139-1.

(3) Novoselov, K. S.; Mishchenko, A.; Carvalho, A.; Castro Neto, A. H. 2D Materials and van Der Waals Heterostructures. *Science* **2016**, *353* (6298). https://doi.org/10.1126/science.aac9439.

(4) Wilson, N. P.; Yao, W.; Shan, J.; Xu, X. Excitons and Emergent Quantum Phenomena in Stacked 2D Semiconductors. *Nature* **2021**, *599* (7885), 383–392. https://doi.org/10.1038/s41586-021-03979-1.

(5) Jiang, Y.; Chen, S.; Zheng, W.; Zheng, B.; Pan, A. Interlayer Exciton Formation, Relaxation, and Transport in TMD van Der Waals Heterostructures. *Light Sci. Appl.* **2021**, *10* (1), 1–29. https://doi.org/10.1038/s41377-021-00500-1.

(6) Hong, X.; Kim, J.; Shi, S.-F.; Zhang, Y.; Jin, C.; Sun, Y.; Tongay, S.; Wu, J.; Zhang, Y.; Wang, F. Ultrafast Charge Transfer in Atomically Thin MoS_2/WS_2 Heterostructures. *Nat. Nanotechnol.* **2014**, *9* (9), 682–686. https://doi.org/10.1038/nnano.2014.167.

(7) Zhang, Z.; Liu, P.; Song, Y.; Hou, Y.; Xu, B.; Liao, T.; Zhang, H. Heterostructure Engineering of 2D Superlattice Materials for Electrocatalysis. **2022**, *2204297*, 1–26. https://doi.org/10.1002/advs.202204297.

(8) He, J.; Reyner, C. J.; Liang, B. L.; Nunna, K.; Huffaker, D. L.; Pavarelli, N.; Gradkowski, K.; Ochalski, T. J.; Huyet, G.; Dorogan, V. G.; Mazur, Yu. I.; Salamo, G. J. Band Alignment Tailoring of $InAs_{1-x}Sb_x$/GaAs Quantum Dots: Control of Type I to Type II Transition. *Nano Lett.* **2010**, *10* (8), 3052–3056. https://doi.org/10.1021/nl102237n.

(9) Nguyen, C. Q.; Ang, Y. S.; Nguyen, S.-T.; Hoang, N. V.; Hung, N. M.; Nguyen, C. V. Tunable Type-II Band Alignment and Electronic Structure of C_3N_4/$MoSi_2N_4$ Heterostructure: Interlayer Coupling and Electric Field. *Phys. Rev. B* **2022**, *105* (4), 045303. https://doi.org/10.1103/PhysRevB.105.045303.

(10) Guo, Z.; Miao, N.; Zhou, J.; Sa, B.; Sun, Z. Strain-Mediated Type-I/Type-II Transition in MXene/Blue Phosphorene van Der Waals Heterostructures for Flexible Optical/Electronic Devices. *J. Mater. Chem. C* **2017**, *5* (4), 978–984. https://doi.org/10.1039/C6TC04349F.

(11) Zhang, S.; Liu, J.; Kirchner, M. M.; Wang, H.; Ren, Y.; Lei, W. Two-Dimensional Heterostructures and Their Device Applications: Progress, Challenges and Opportunities—Review. *J. Phys. Appl. Phys.* **2021**, *54* (43), 433001. https://doi.org/10.1088/1361-6463/ac16a4.

(12) Qi, J.; Wu, Z.; Wang, W.; Bao, K.; Wang, L.; Wu, J.; Ke, C.; Xu, Y.; He, Q. Fabrication and Applications of van Der Waals Heterostructures. *Int. J. Extreme Manuf.* **2023**, *5* (2), 022007. https://doi.org/10.1088/2631-7990/acc8a1.

(13) Saparov, B.; Mitzi, D. B. Organic–Inorganic Perovskites: Structural Versatility for Functional Materials Design. *Chem. Rev.* **2016**, *116* (7), 4558–4596. https://doi.org/10.1021/acs.chemrev.5b00715.

(14) Ishihara, T.; Takahashi, J.; Goto, T. Exciton State in Two-Dimensional Perovskite Semiconductor $(C_{10}H_{21}NH_3)_2PbI_4$. *Solid State Commun.* **1989**, *69* (9), 933–936. https://doi.org/10.1016/0038-1098(89)90935-6.

(15) Ishihara, T. Optical Properties of PbI-Based Perovskite Structures. *J. Lumin.* **1994**, *60–61*, 269–274. https://doi.org/10.1016/0022-2313(94)90145-7.

(16) Dohner, E. R.; Hoke, E. T.; Karunadasa, H. I. Self-Assembly of Broadband White-Light Emitters. *J. Am. Chem. Soc.* **2014**, *136* (5), 1718–1721. https://doi.org/10.1021/ja411045r.

(17) Smith, M. D.; Connor, B. A.; Karunadasa, H. I. Tuning the Luminescence of Layered Halide Perovskites. *Chemical Reviews*. American Chemical Society March 13, 2019, pp 3104–3139. https://doi.org/10.1021/acs.chemrev.8b00477.

(18) Tanaka, K.; Takahashi, T.; Kondo, T.; Umeda, K.; Ema, K.; Umebayashi, T.; Asai, K.; Uchida, K.; Miura, N. Electronic and Excitonic Structures of Inorganic–Organic Perovskite-Type Quantum-Well Crystal $(C_4H_9NH_3)_2PbBr_4$. *Jpn. J. Appl. Phys.* **2005**, *44* (8R), 5923. https://doi.org/10.1143/JJAP.44.5923.

(19) Wang, K.; Jin, L.; Gao, Y.; Liang, A.; Finkenauer, B. P.; Zhao, W.; Wei, Z.; Zhu, C.; Guo, T.-F.; Huang, L.; Dou, L. Lead-Free Organic–Perovskite Hybrid Quantum Wells for Highly Stable Light-Emitting Diodes. *ACS Nano* **2021**, *15* (4), 6316–6325. https://doi.org/10.1021/acsnano.1c00872.

(20) Braun, M.; Tuffentsammer, W.; Wachtel, H.; Wolf, H. C. Tailoring of Energy Levels in Lead Chloride Based Layered Perovskites and Energy Transfer between the Organic and Inorganic Planes. *Chem. Phys. Lett.* **1999**, *303* (1–2), 157–164. https://doi.org/10.1016/S0009-2614(99)00205-5.

(21) Mitzi, D. B.; Chondroudis, K.; Kagan, C. R. Design, Structure, and Optical Properties of Organic-Inorganic Perovskites Containing an Oligothiophene Chromophore. *Inorg. Chem.* **1999**, *38* (26), 6246–6256. https://doi.org/10.1021/ic991048k.

(22) Gao, Y.; Shi, E.; Deng, S.; Shiring, S. B.; Snaider, J. M.; Liang, C.; Yuan, B.; Song, R.; Janke, S. M.; Liebman-Peláez, A.; Yoo, P.; Zeller, M.; Boudouris, B. W.; Liao, P.; Zhu, C.; Blum, V.; Yu, Y.; Savoie, B. M.; Huang, L.; Dou, L. Molecular Engineering of Organic–Inorganic Hybrid Perovskites Quantum Wells. *Nat. Chem.* **2019**, *11* (12), 1151–1157. https://doi.org/10.1038/s41557-019-0354-2.

(23) Sun, J.; Wang, K.; Ma, K.; Park, J. Y.; Lin, Z.-Y.; Savoie, B. M.; Dou, L. Emerging Two-Dimensional Organic Semiconductor-Incorporated Perovskites─A Fascinating Family of Hybrid Electronic Materials. *J. Am. Chem. Soc.* **2023**, *145* (38), 20694–20715. https://doi.org/10.1021/jacs.3c02143.

(24) Aubrey, M. L.; Saldivar Valdes, A.; Filip, M. R.; Connor, B. A.; Lindquist, K. P.; Neaton, J. B.; Karunadasa, H. I. Directed Assembly of Layered Perovskite Heterostructures as Single Crystals. *Nature* **2021**, *597* (7876), 355–359. https://doi.org/10.1038/s41586-021-03810-x.

(25) Caniglia, C. D.; Li, Y.; Wen, J.; Brueggemeyer, M. T.; Lee, Y. S.; Solomon, E. I.; Fisher, I. R.; Karunadasa, H. I. Isolation of Diamond Spin Chains in a Layered Halide Perovskite Heterostructure. *J. Am. Chem. Soc.* **2025**, *147* (31), 28340–28349. https://doi.org/10.1021/jacs.5c08981.

(26) Jaffe, A.; Lin, Y.; Karunadasa, H. I. Halide Perovskites under Pressure: Accessing New Properties through Lattice Compression. *ACS Energy Lett.* **2017**, *2* (7), 1549–1555. https://doi.org/10.1021/acsenergylett.7b00284.

(27) Mercier, N.; Riou, A. An Organic–Inorganic Hybrid Perovskite Containing Copper Paddle-Wheel Clusters Linking Perovskite Layers : $[Cu(O_2C–(CH_2)_3–NH_3)_2]PbBr_4$. *Chem. Commun.* **2004**, No. 7, 844–845. https://doi.org/10.1039/B316847F.

(28) Sun, C.; Li, Y.; Yin, J.; Li, D.; Wu, C.; Zhang, C.; Fei, H. Highly Stable MOF-Type Lead Halide Luminescent Ferroelectrics Angewandte. **2024**, *200092*. https://doi.org/10.1002/anie.202407102.

(29) Yin, J.; Yang, H.; Fei, H. Robust, Cationic Lead Halide Layered Materials with Efficient Broadband White-Light Emission. *Chem Mater* **2019**, *31*, 31. https://doi.org/10.1021/acs.chemmater.8b05345.

(30) Kepenekian, M.; Robles, R.; Katan, C.; Sapori, D.; Pedesseau, L.; Even, J. Rashba and Dresselhaus Effects in Hybrid Organic-Inorganic Perovskites: From Basics to Devices. *ACS Nano* **2015**, *9* (12), 11557–11567. https://doi.org/10.1021/acsnano.5b04409.

(31) Krach, S.; Forero-Correa, N.; Biega, R. I.; Reyes-Lillo, S. E.; Leppert, L. Emergence of Rashba-/Dresselhaus Effects in Ruddlesden-Popper Halide Perovskites with Octahedral Rotations. *J. Phys. Condens. Matter* **2023**, *35* (17). https://doi.org/10.1088/1361-648X/acbd0c.

(32) Zeleňák, V.; Vargová, Z.; Györyová, K. Correlation of Infrared Spectra of Zinc(II) Carboxylates with Their Structures. *Spectrochim. Acta. A. Mol. Biomol. Spectrosc.* **2007**, *66* (2), 262–272. https://doi.org/10.1016/j.saa.2006.02.050.

(33) Smith, M. D.; Jaffe, A.; Dohner, E. R.; Lindenberg, A. M.; Karunadasa, H. I. Structural Origins of Broadband Emission from Layered Pb–Br Hybrid Perovskites. *Chem. Sci.* **2017**, *8* (6), 4497–4504. https://doi.org/10.1039/C7SC01590A.

(34) Li, X.-N.; Li, P.-F.; Liao, W.-Q.; Ge, J.-Z.; Wu, D.-H.; Ye, H.-Y. Phase-Transition and Photoluminescence Properties of a Hybrid Layered Perovskite: Bis[(Cyclohexylmethyl)Ammonium] Tetrabromidolead(II). *Eur. J. Inorg. Chem.* **2017**, *2017* (5), 938–942. https://doi.org/10.1002/ejic.201601269.

(35) Crace, E. J.; Su, A. C.; Karunadasa, H. I. Reliably Obtaining White Light from Layered Halide Perovskites at Room Temperature. *Chem. Sci.* **2022**, *13* (34), 9973–9979. https://doi.org/10.1039/d2sc02381d.

(36) Dohner, E. R.; Jaffe, A.; Bradshaw, L. R.; Karunadasa, H. I. Intrinsic White-Light Emission from Layered Hybrid Perovskites. *J. Am. Chem. Soc.* **2014**, *136* (38), 13154–13157. https://doi.org/10.1021/ja507086b.

(37) Hu, T.; Smith, M. D.; Dohner, E. R.; Sher, M.; Wu, X.; Trinh, M. T.; Fisher, A.; Corbett, J.; Zhu, X.; Karunadasa, H. I.; Lindenberg, A. M. Mechanism for Broadband White-Light Emission from Two- Dimensional (110) Hybrid Perovskites. **2016**, No. 110. https://doi.org/10.1021/acs.jpclett.6b00793.

(38) Hohenberg, P.; Kohn, W. Inhomogeneous Electron Gas. *Phys. Rev.* **1964**, *136* (3B), B864–B871. https://doi.org/10.1103/PhysRev.136.B864.

(39) Perdew, J. P.; Burke, K.; Ernzerhof, M. Generalized Gradient Approximation Made Simple. *Phys. Rev. Lett.* **1996**, *77* (18), 3865–3868. https://doi.org/10.1103/PhysRevLett.77.3865.

(40) Hinuma, Y.; Pizzi, G.; Kumagai, Y.; Oba, F.; Tanaka, I. Band Structure Diagram Paths Based on Crystallography. *Comput. Mater. Sci.* **2017**, *128*, 140–184. https://doi.org/10.1016/j.commatsci.2016.10.015.

(41) Grimme, S.; Antony, J.; Ehrlich, S.; Krieg, H. A Consistent and Accurate Ab Initio Parametrization of Density Functional Dispersion Correction (DFT-D) for the 94 Elements H-Pu. *J. Chem. Phys.* **2010**, *132* (15), 154104. https://doi.org/10.1063/1.3382344.

(42) Hybertsen, M. S.; Louie, S. G. Electron Correlation in Semiconductors and Insulators: Band Gaps and Quasiparticle Energies. *Phys. Rev. B* **1986**, *34* (8), 5390–5413. https://doi.org/10.1103/PhysRevB.34.5390.

(43) Deslippe, J.; Samsonidze, G.; Strubbe, D. A.; Jain, M.; Cohen, M. L.; Louie, S. G. BerkeleyGW: A Massively Parallel Computer Package for the Calculation of the Quasiparticle and Optical Properties of Materials and Nanostructures. *Comput. Phys. Commun.* **2012**, *183* (6), 1269–1289. https://doi.org/10.1016/j.cpc.2011.12.006.

(44) Rohlfing, M.; Louie, S. G. Electron-Hole Excitations in Semiconductors and Insulators. *Phys. Rev. Lett.* **1998**, *81* (11), 2312–2315. https://doi.org/10.1103/PhysRevLett.81.2312.

(45) Rohlfing, M.; Louie, S. G. Electron-Hole Excitations and Optical Spectra from First Principles. *Phys. Rev. B* **2000**, *62* (8), 4927–4944. https://doi.org/10.1103/PhysRevB.62.4927.

(46) Filip, M. R.; Leppert, L. Halide Perovskites from First Principles: From Fundamental Optoelectronic Properties to the Impact of Structural and Chemical Heterogeneity. *Electron. Struct.* **2024**, *6* (3), 033002. https://doi.org/10.1088/2516-1075/ad5898.

(47) Gant, S. E.; Haber, J. B.; Filip, M. R.; Sagredo, F.; Wing, D.; Ohad, G.; Kronik, L.; Neaton, J. B. Optimally Tuned Starting Point for Single-Shot *GW* Calculations of Solids. *Phys. Rev. Mater.* **2022**, *6* (5), 053802. https://doi.org/10.1103/PhysRevMaterials.6.053802.

(48) Ohad, G.; Wing, D.; Gant, S. E.; Cohen, A. V.; Haber, J. B.; Sagredo, F.; Filip, M. R.; Neaton, J. B.; Kronik, L. Band Gaps of Halide Perovskites from a Wannier-Localized Optimally Tuned Screened Range-Separated Hybrid Functional. *Phys. Rev. Mater.* **2022**, *6* (10), 104606. https://doi.org/10.1103/PhysRevMaterials.6.104606.

(49) Filip, M. R.; Qiu, D. Y.; Del Ben, M.; Neaton, J. B. Screening of Excitons by Organic Cations in Quasi-Two-Dimensional Organic–Inorganic Lead-Halide Perovskites. *Nano Lett.* **2022**, *22* (12), 4870–4878. https://doi.org/10.1021/acs.nanolett.2c01306.

(50) Sharifzadeh, S.; Darancet, P.; Kronik, L.; Neaton, J. B. Low-Energy Charge-Transfer Excitons in Organic Solids from First-Principles: The Case of Pentacene. *J. Phys. Chem. Lett.* **2013**, *4* (13), 2197–2201. https://doi.org/10.1021/jz401069f.

(51) Chen, Y.; Filip, M. R. Tunable Interlayer Delocalization of Excitons in Layered Organic − Inorganic Halide Perovskites. **2023**. https://doi.org/10.1021/acs.jpclett.3c02339.

(52) Simon, F.; Clevers, S.; Dupray, V.; Coquerel, G. Relevance of the Second Harmonic Generation to Characterize Crystalline Samples. *Chem. Eng. Technol.* **2015**, *38* (6), 971–983. https://doi.org/10.1002/ceat.201400756.

(53) Dehnhardt, N.; Axt, M.; Zimmermann, J.; Yang, M.; Mette, G.; Heine, J. Band Gap-Tunable, Chiral Hybrid Metal Halides Displaying Second-Harmonic Generation. *Chem. Mater.* **2020**, *32* (11), 4801–4807. https://doi.org/10.1021/acs.chemmater.0c01605.

(54) Li, Y.; Rao, Y.; Mak, K. F.; You, Y.; Wang, S.; Dean, C. R.; Heinz, T. F. Probing Symmetry Properties of Few-Layer MoS_2 and h-BN by Optical Second-Harmonic Generation. *Nano Lett.* **2013**, *13* (7), 3329–3333. https://doi.org/10.1021/nl401561r.

(55) Yuan, C.; Li, X.; Semin, S.; Feng, Y.; Rasing, T.; Xu, J. Chiral Lead Halide Perovskite Nanowires for Second-Order Nonlinear Optics. *Nano Lett.* **2018**, *18* (9), 5411–5417. https://doi.org/10.1021/acs.nanolett.8b01616.

(56) Hagimoto, K.; Mito, A. Determination of the Second-Order Susceptibility of Ammonium Dihydrogen Phosphate and α-Quartz at 633 and 1064 Nm. *Appl. Opt.* **1995**, *34* (36), 8276–8282. https://doi.org/10.1364/AO.34.008276.

(57) Wei, W. J.; Jiang, X. X.; Dong, L. Y.; Liu, W. W.; Han, X. B.; Qin, Y.; Li, K.; Li, W.; Lin, Z. S.; Bu, X. H.; Lu, P. X. Regulating Second-Harmonic Generation by van Der Waals Interactions in Two-Dimensional Lead Halide Perovskite Nanosheets. *J. Am. Chem. Soc.* **2019**, *141* (23), 9134–9139. https://doi.org/10.1021/jacs.9b01874.

(58) Sun, Z.; Liu, X.; Khan, T.; Ji, C.; Asghar, M. A.; Zhao, S.; Li, L.; Hong, M.; Luo, J. A Photoferroelectric Perovskite-Type Organometallic Halide with Exceptional Anisotropy of Bulk Photovoltaic Effects. *Angew. Chem. Int. Ed.* **2016**, *55* (22), 6545–6550. https://doi.org/10.1002/anie.201601933.

(59) Okorogu, A. O.; Mirov, S. B.; Lee, W.; Crouthamel, D. I.; Jenkins, N.; Dergachev, A. Y.; Vodopyanov, K. L.; Badikov, V. V. Tunable Middle Infrared Downconversion in GaSe and $AgGaS_2$. *Opt.*

Commun. **1998**, *155* (4), 307–312. https://doi.org/10.1016/S0030-4018(98)00397-6.

(60) Dang, Y.; Liu, X.; Cao, B.; Tao, X. Chiral Halide Perovskite Crystals for Optoelectronic Applications. *Matter* **2021**, *4* (3), 794–820. https://doi.org/10.1016/j.matt.2020.12.018.

(61) Fedoruk, K.; Drozdowski, D.; Maczka, M.; Zareba, J. K.; Stefańska, D.; Gagor, A.; Sieradzki, A. $[Methylhydrazinium]_2PbCl_4$, a Two-Dimensional Perovskite with Polar and Modulated Phases. *Inorg. Chem.* **2022**, *61* (39), 15520–15531. https://doi.org/10.1021/acs.inorgchem.2c02206.

(62) Zheng, Y.; Xu, J.; Bu, X.-H. 1D Chiral Lead Halide Perovskites with Superior Second-Order Optical Nonlinearity. *Adv. Opt. Mater.* **2022**, *10* (1), 2101545. https://doi.org/10.1002/adom.202101545.

(63) Du, K.; Tu, Q.; Zhang, X.; Han, Q.; Liu, J.; Zauscher, S.; Mitzi, D. B. Two-Dimensional Lead(II) Halide-Based Hybrid Perovskites Templated by Acene Alkylamines: Crystal Structures, Optical Properties, and Piezoelectricity. *Inorg. Chem.* **2017**, *56* (15), 9291–9302. https://doi.org/10.1021/acs.inorgchem.7b01094.

(64) Zhang, T.; Liu, X.; Zhou, J.; Liu, J. Two Organic Hybrid Iodoplumbates Directed by a Bifunctional Bis(Pyrazinyl)Triazole. *Inorg. Chem.* **2021**, *60* (7), 5362–5366. https://doi.org/10.1021/acs.inorgchem.1c00330.

(65) Hua, X.-N.; Liao, W.-Q.; Tang, Y.-Y.; Li, P.-F.; Shi, P.-P.; Zhao, D.; Xiong, R.-G. A Room-Temperature Hybrid Lead Iodide Perovskite Ferroelectric. *J. Am. Chem. Soc.* **2018**, *140* (38), 12296–12302. https://doi.org/10.1021/jacs.8b08286.

(66) Zhang, H.-Y.; Song, X.-J.; Chen, X.-G.; Zhang, Z.-X.; You, Y.-M.; Tang, Y.-Y.; Xiong, R.-G. Observation of Vortex Domains in a Two-Dimensional Lead Iodide Perovskite Ferroelectric. *J. Am. Chem. Soc.* **2020**, *142* (10), 4925–4931. https://doi.org/10.1021/jacs.0c00371.

(67) Moqbel, R.; Nanae, R.; Kitamura, S.; Lee, M.; Lan, Y.; Lee, C.; Nagashio, K.; Lin, K. Giant Second-Order Nonlinearity and Anisotropy of Large-Sized Few-Layer SnS with Ferroelectric Stacking. *Adv. Opt. Mater.* **2024**, *12* (19), 1–10. https://doi.org/10.1002/adom.202400355.

(68) Denev, S. A.; Lummen, T. T. A.; Barnes, E.; Kumar, A.; Gopalan, V. Probing Ferroelectrics Using Optical Second Harmonic Generation. *J. Am. Ceram. Soc.* **2011**, *94* (9), 2699–2727. https://doi.org/10.1111/j.1551-2916.2011.04740.x.

TOC GRAPHIC

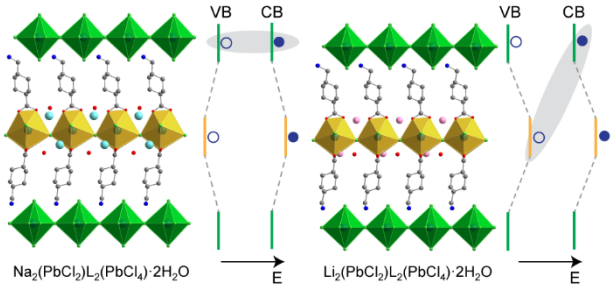
VB
CB
VB
CB
$Na_2(PbCl_2)L_2(PbCl_4)\cdot 2H_2O$
E
$Li_2(PbCl_2)L_2(PbCl_4)\cdot 2H_2O$
E